First demonstration of intrafractional tumor-tracked irradiation using 2D phantom MR images on a prototype linac-MR

Jihyun Yun
Department of Physics, University of Alberta, 11322-89 Avenue, Edmonton, Alberta T6G 2G7, Canada and Department of Oncology, Medical Physics Division, University of Alberta, 11560 University Avenue, Edmonton, Alberta T6G 1Z2, Canada

Keith Wachowicz, Marc Mackenzie, Satyapal Rathee, and Don Robinson
Department of Medical Physics, Cross Cancer Institute, 11560 University Avenue, Edmonton, Alberta T6G 1Z2, Canada and Department of Oncology, Medical Physics Division, University of Alberta, 11560 University Avenue, Edmonton, Alberta T6G 1Z2, Canada

B. G. Fallone[a)]
Department of Physics, University of Alberta, 11322-89 Avenue, Edmonton, Alberta T6G 2G7, Canada; Department of Medical Physics, Cross Cancer Institute, 11560 University Avenue, Edmonton, Alberta T6G 1Z2, Canada; and Department of Oncology, Medical Physics Division, University of Alberta, 11560 University Avenue, Edmonton, Alberta T6G 1Z2, Canada

(Received 16 November 2012; revised 19 February 2013; accepted for publication 8 April 2013; published 30 April 2013)

Purpose: To demonstrate intrafractional MR tumor tracking using a prototype linac-MR by delivering radiation to a moving target undergoing simulated tumor motions.
Methods: A prototype linac-MR at the Cross Cancer Institute was used for intrafractional MR imaging and simultaneous beam delivery. A Varian 52-leaf MK-II multileaf collimator (MLC) was used for beam collimation. The authors used an inhouse built MR compatible motion phantom to simulate tumor motions during tracking with two different motion patterns (sine and modified cosine). Gafchromic film was inserted in the phantom to measure radiation exposure, and this film measurement was converted to dose (cGy) for further analysis. The authors demonstrated intrafractional tracking in various scenarios: [Scenario 0 (S0)] no phantom motion + no beam margin, (S1) no phantom motion + maximum beam margin, (S2) phantom motion + no beam margin, (S3) S2 + MLC tracking, and (S4) S3 + motion prediction. S0 emulates a perfect tumor tracking scenario, and its result was used as a "gold-standard" to evaluate tracking accuracy from other scenarios. The authors compared (1) time difference in phantom and MLC motion curves in S3 and S4, and (2) dose profiles (50% beam width, 80%–20% penumbra width) from scenarios S1–S4 to S0.
Results: In S4, no observable time difference exists between the phantom and MLC motion curves, indicating that MLC tracks phantom motion accurately. Comparing S4 to S0, 50% beam width reveals minimal differences of < 0.5 mm, while the increase in 80%–20% penumbra width is limited to 0.4 and 1.7 mm in the sine and modified cosine patterns, respectively.
Conclusions: The authors report the first demonstration of intrafractional tumor tracking using 2D MR images. During 2 min of tracking, the authors delivered highly conformal dose to a moving target that simulates tumor motions. Compared to static target irradiation, the 50% beam width remains essentially the same (within 0.5 mm), with an increase in 80%–20% penumbra width of less than 1.7 mm in moving target irradiation. These results illustrate potential dosimetric advantages of intrafractional MR tumor tracking in treating mobile tumors as shown for the phantom case. © *2013 American Association of Physicists in Medicine*. [http://dx.doi.org/10.1118/1.4802735]

Key words: intrafraction motion management, lung-tumor tracking, linac-MR, MRI guidance, organ motion compensation

I. INTRODUCTION

Intrafractional tracking of mobile tumors is of considerable interest. Several groups are investigating intrafractional tumor tracking systems[1–3] to deliver highly conformal radiation dose to mobile tumors. Krauss *et al.*[4] and Sawant *et al.*[2] have performed phantom studies demonstrating the feasibility of 2D intrafractional lung-tumor tracking. In these studies, a tumor surrogate was driven according to a sinusoidal trajectory and its position was detected using a monitoring system developed by Calypso Medical Technologies (Seattle, WA). Cho *et al.*[3] suggested the simultaneous use of kV/MV imaging for 3D intrafractional tracking, where a gold marker was used as a tumor surrogate. Also, commercial systems perform intrafractional tumor tracking using different types of tumor surrogates.[5–7]

Despite the wide variety of tracking techniques, all current tracking methods utilize indirect tracking through the use of internal and/or external tumor surrogates. Reliance on surrogates, however, has been shown to be problematic for accurate

tumor tracking for the following reasons: (1) implanted seeds, for liver and prostate tumors,[8] have been shown to migrate by 5.1 and 4.5 mm from their initial positions, respectively. In some cases, the seeds might be completely dislodged during the course of the radiation treatment. Imura *et al.*,[9] in a study of 57 patients, reported that 25% of total surrogates was lost during the course of lung-tumor treatments; (2) tracking using external surrogates assumes good correlations between internal tumor motion and external surrogate displacement, whereas mismatches between tumor and surrogates up to 9 mm have been shown;[10,11] and (3) any deformation of tumor shape is completely unknown during tracking. Moreover, since the implanted seeds are usually placed only within the tumor, the motion of the nearby soft-tissue and healthy organs, and their relationship to the tumor, are not known during tracking. Therefore, to account for the uncertainty in correlation between tumor position and surrogates, extended regions surrounding the lesion must be irradiated in order to ensure sufficient target coverage.[12]

Although modern imaging systems can provide 3D or 4D anatomical information, all imaging systems are still surrogates to the actual tumor shape, size, and location. In 2008, it was claimed that the imaging modalities used in cancer treatment must be improved by 3–4 orders of magnitude in terms of their tumor-to-background ratio, in order to make meaningful impact on cancer treatment.[13] While the improvements of imaging systems are in progress, the limitations of relying on imaging in radiation treatment need to be acknowledged.

In contemporary radiation treatment process, computed tomography (CT) based target definition is the standard of care. However, large efforts have been made to incorporate magnetic resonance imaging (MRI) in target definition due to its superior soft tissue contrast that enables to visualize tumor extent in more detail.[14,15] A recent study investigated the dose calculation accuracy for different tumor sites (lung, prostate, brain, head, and neck) from 40 patients using MRI data, and compared it to CT based treatment plans. Here, the target volume was defined on MR images and registered to the CT images. Whether the treatment plan was based on CT or MRI, this study showed that nearly the same number of monitor units (<1.6% difference) were required to deliver the prescribed dose.[16]

Our group at the Cross Cancer Institute reported the first integrated radiotherapy-MR system known as a linac-MR.[17] With this system we have investigated the requirements for MR-based intrafractional tumor tracking. These requirements include (1) characterization of multileaf collimator (MLC) motor operation in an external magnetic field,[18] (2) measurement of radio frequency (RF) noise from MLC and shielding technique,[19] (3) development of lung-tumor autocontouring[20] software compatible with MR images, and (4) development of lung-tumor motion prediction software for MR-based tracking.[21]

We have focused on lung-tumor tracking due to the potential for a large range of motion during treatment delivery. Various studies have shown that lung-tumor may move up to 40 mm in superior-inferior (SI), 15 mm in anterior-posterior (AP), and 10 mm in left-right (LR) directions during normal breathing.[22–24] Volume changes up to 20% and rotations up to 50° with respect to each axis have also been reported.[25] Several methods have been used to reduce the range of respiratory motion in radiotherapy, including active-breathing control (ABC) or forced shallow breathing with abdominal compression (FSB).[26] In ABC, the patient must follow the breathing instructions, thus many infirm patients may have difficulties to comply. FSB may cause problems for the patients with particularly poor pulmonary function, and those with percutaneous gastrostomy tube. Similarly, the patients with large abdominal aortic aneurysms may not be suitable for FSB.[27] Because it is not always possible to apply the methods of respiratory motion reduction, we focused on tracking lung-tumor motions during normal breathing.

In this study, we report the first physical demonstration of intrafractional tumor tracking using 2D MR images that is built upon our previous investigations.[18–21] An MR compatible motion phantom was used to simulate tumor motion during beam delivery. We present our experimental setup, different tracking scenarios that we tested, and their results.

II. MATERIALS AND METHODS

II.A. Experimental setup

II.A.1. Linac-MR and MLC

Figure 1 shows our setup for tracking experiments. We used a prototype linac-MR for intrafractional MR imaging and simultaneous beam delivery. A Varian 52-leaf MK-II MLC was used for beam collimation during tracking, which was controlled by inhouse built software and electronics. In this study, ten MLC leaves (five in each carriage, MLC-L and MLC-R in Fig. 1) were used for tracking.

All MR images were acquired using a balanced steady state free precession (bSSFP) technique in the beam's eye view (BEV) plane (FOV = 256 × 192 mm, 2 × 2 × 30 mm^3, TE = 1.3 ms, TR = 2.6 ms, dynamic scan time = 250 ms, i.e., 4 fps). A top down view of MR imaging slice is indicated in Fig. 1(a), which is at the center of the magnet and perpendicular to the beam. A sample sequence used to perform tracking in this study is shown in Fig. 2. More details regarding bSSFP sequence can be found in Bernstein.[28]

II.A.2. MR compatible motion phantom

Figure 1 illustrates the phantom setup during tracking experiments. A more detailed phantom design is shown in Fig. 3. Our phantom was driven by a programmable motor using a shaft that is both nonmagnetic and nonconductive to create 1D motion along the axis of the RF coil as indicated in Fig. 3(d). This creates phantom motion in the direction perpendicular to the x-ray beam along the leaf motion direction of the MLC.

This phantom is made of two symmetrical parts as shown in Fig. 3(a). Here, the central custom-shaped target represents a tumor volume, which is composed of 70 g/l of porcine skin gelatin containing approximately 10 mM of aqueous copper sulfate ($CuSO_4$:$5H_2O$) and 0.1% sodium benzoate

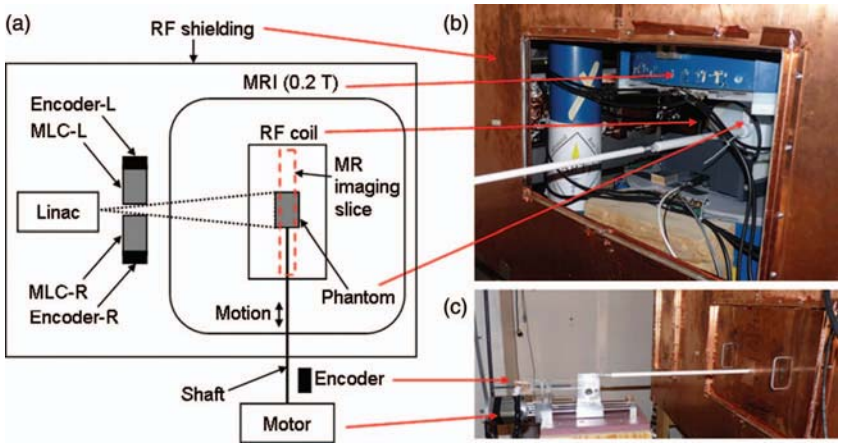

FIG. 1. Experimental setup: (a) brief diagram of entire setup (top down view), (b) prototype linac-MR and phantom setting with RF cage open, (c) side view with RF cage closed.

($NaC_6H_5CO_2$). T_1 and T_2 values of the target material were measured to be approximately 22 and 16 ms, respectively. Copper sulfate was added to reduce the relaxation times of the gel, which allowed for better-quality T_1-weighted imaging used extensively for scouting. Sodium benzoate was added as a preservative. Density of the target material was measured to be 0.99 g/ml, which is very similar to water. Because the target material is mostly composed of water with a small amount of skin gelatin, the effective atomic number of the target material should be equal to that of water, which is known to be 3.4.[29] A small impact of this material on the dose delivered to the film does not influence the result of this study, because film comparisons are all relative. In *in vivo* MR images using the bSSFP sequence, the lung background is darker than the tumor.[30] For our phantom, the target is embedded in a polystyrene case that contributes no MR signal in the bSSFP imaging sequence generating darker background to the target, and provides a rigid casing to contain the target material.

We inserted Gafchromic EBT2 film (International Specialty Products, Wayne, NJ) between the two cases to measure radiation exposure during tracking. To compare radiation exposures in different films, the following registration technique was used. Prior to irradiation, each film was placed and fixed on the case as shown in Fig. 3(a). Then, we visually inspected the eight inner corners of the phantom shape and manually marked them on the film using permanent ink. These are referred as surrogate markers as indicated by red dots in Fig. 3(a).

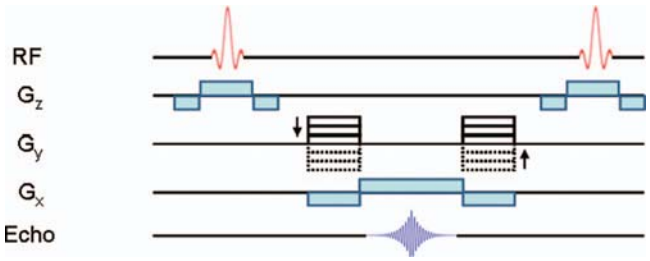

FIG. 2. Sample bSSFP sequence used to perform tracking in this study.

Figure 3(b) shows the phantom in its assembled state. An MR image of this phantom acquired during the tracking experiment is shown in Fig. 3(c) illustrating the MR signal from the gelatin "tumor" surrounded by background signal. This image was taken while the phantom and MLC were in motion during beam delivery. RF noise from the MLC is shielded using the method developed in a previous study.[19] Figure 3(d) shows the phantom and RF coil placed in the linac-MR.

II.A.3. MLC and phantom position monitoring during tracking

Each MLC leaf is driven by a DC servo motor located in the back of the carriage. Each motor has a magnetic encoder that detects rotor position, which in turn, provides leaf position. Hence, ten encoders (five in each carriage, Encoder-L and Encoder-R in Fig. 1) were used to sense and monitor leaf motions in this study. The DC servo motors were controlled by motor drivers programmed through LabVIEW scripts (LabVIEW 2011, National Instruments, Austin, TX) implemented on a field programmable gate arrays (FPGA) chip.

Our motion phantom has an optical encoder (Fig. 1) placed on the shaft that measures phantom position. The optical encoder reading was primary feedback to a separate motor driver that was programmed to control phantom motions.

During the tracking experiments, we recorded all encoder readings from each MLC leaf and the phantom. All encoder readings were taken at the same instance every 50 ms and time-stamped using an internal clock (millisecond resolution) in the LabVIEW software.

II.A.4. Tumor motion simulation

We drove our phantom following a preprogrammed motion pattern during the tracking experiments. The phantom was moving in the read encoding direction. The speed of phantom when the image was taken depends on the asynchronous phase of motion pattern, ranges from 0 to 3.1 cm/s. Two different motion patterns were used in this study to simulate

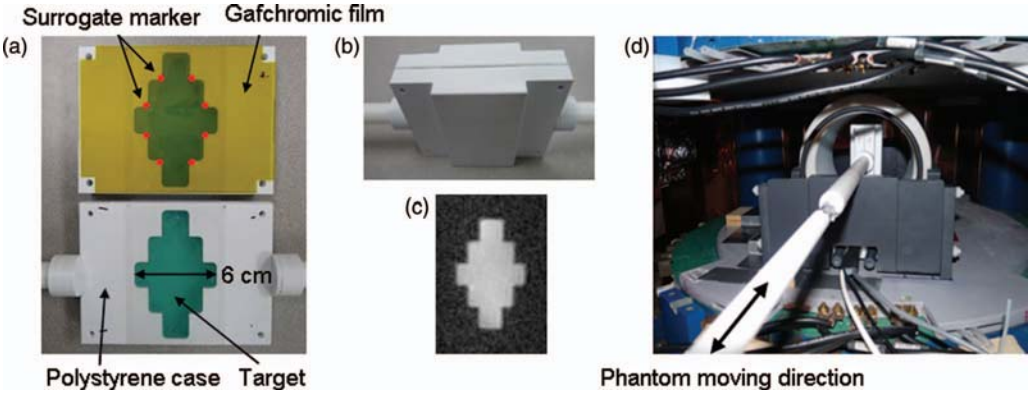

FIG. 3. Motion phantom: (a) phantom parts, (b) assembled phantom, (c) MR image during tracking and beam delivery, (d) phantom and RF coil placed in the linac-MR.

tumor motions: (1) a sine pattern (period: 6.7 s, motion range: 4 cm, max. speed: 1.8 cm/s) representing ideal, periodic tumor motions, and (2) a modified cosine pattern (period: 5.1 s, motion range: 4 cm, max. speed: 3.1 cm/s), following the form $y(t) = a \cdot \cos^4(t) + b$, which represents more realistic lung-tumor motions with time t and constants a and b. Lujan *et al.*[31] suggested the modified cosine pattern to model breathing motions, which is shown to be related to abdominal tumor motions including lung-tumors.[32] These two patterns have been used in previous studies to validate surrogate based tracking systems.[1–4] The motion range and period of these motion patterns were determined in reference to the previously reported lung-tumor motions in the SI directions.[22,23] Specifically, the motion range was selected from the extreme end of the spectrum to challenge the tracking system.

II.A.5. Beam calibration to MR images

As shown in Fig. 1(a), MLC is the only beam compensator/collimator used in the linac-MR. The relationship between MLC leaf positions and corresponding beam shape and position at the imaging slice indicated in Fig. 1(a) was established through film measurements. Based on this, we performed the following steps to calibrate the radiation beam to MR images.

First, MR images were acquired when the phantom was placed at three known locations within the imaging plane: (1) at the center of the magnet (i.e., equilibrium position), (2) 2 cm inward from the equilibrium position along the motion direction in Fig. 1(a), and (3) 2 cm outward from the equilibrium position. The 2 cm displacement was chosen to encompass the potential motion range of the phantom used in this study.

Second, we controlled the MLC to conform the radiation beam to the target shown in the MR images at the above three locations. The accurate beam shape concordance with MR image was confirmed with film measurements. From this, we established the relationship between the imaging coordinates of the MRI and MLC leaf positions for three different locations in the imaging plane.

The MLC leaf positions for any other possible locations tracked using the intrafractional MR images were calculated by linear interpolation between the three calibration points.

II.B. Software development for intrafractional tumor tracking

II.B.1. Autocontouring software

An autocontouring software used in this study is based on our previously developed autocontouring algorithm,[20] which determines both the shape and position (i.e., centroid) of a tumor from each intrafractional MR image in less than 5 ms. The software was developed to perform with 2D MR images. There exist five parameters that may impact the accuracy of autocontouring within this software, thus the values of these parameters must be determined prior to autocontouring. Parameter optimization uses images that are acquired prior to tracking and contain the outlined target. The autocontouring software is fully automatic in its determination of the parameters as indicated in Sec. II.A.1.b of our previous publication.[20] More discussions regarding the parameter optimization process in this study follow in Sec. II.C.1 of this report.

II.B.2. System delay and motion prediction software

System delay is the time interval between the detection of current tumor position data (i.e., image acquisition) and the beam delivery upon the MLC reaching the target position. In our tracking method using the linac-MR, system delay is comprised of image acquisition, image processing, and MLC motion times.

To determine the amount of system delay, we performed tumor tracking without a motion prediction capability using both motion patterns. During this test, the positional changes of the phantom and MLC were monitored via the optical and magnetic encoders reading, respectively, as explained in Sec. II.A.3. These motion data were plotted as a function of time, and we calculated system delay from the time difference between the two curves. The result was used as input to our motion prediction software as shown in Step 6 in Fig. 4.

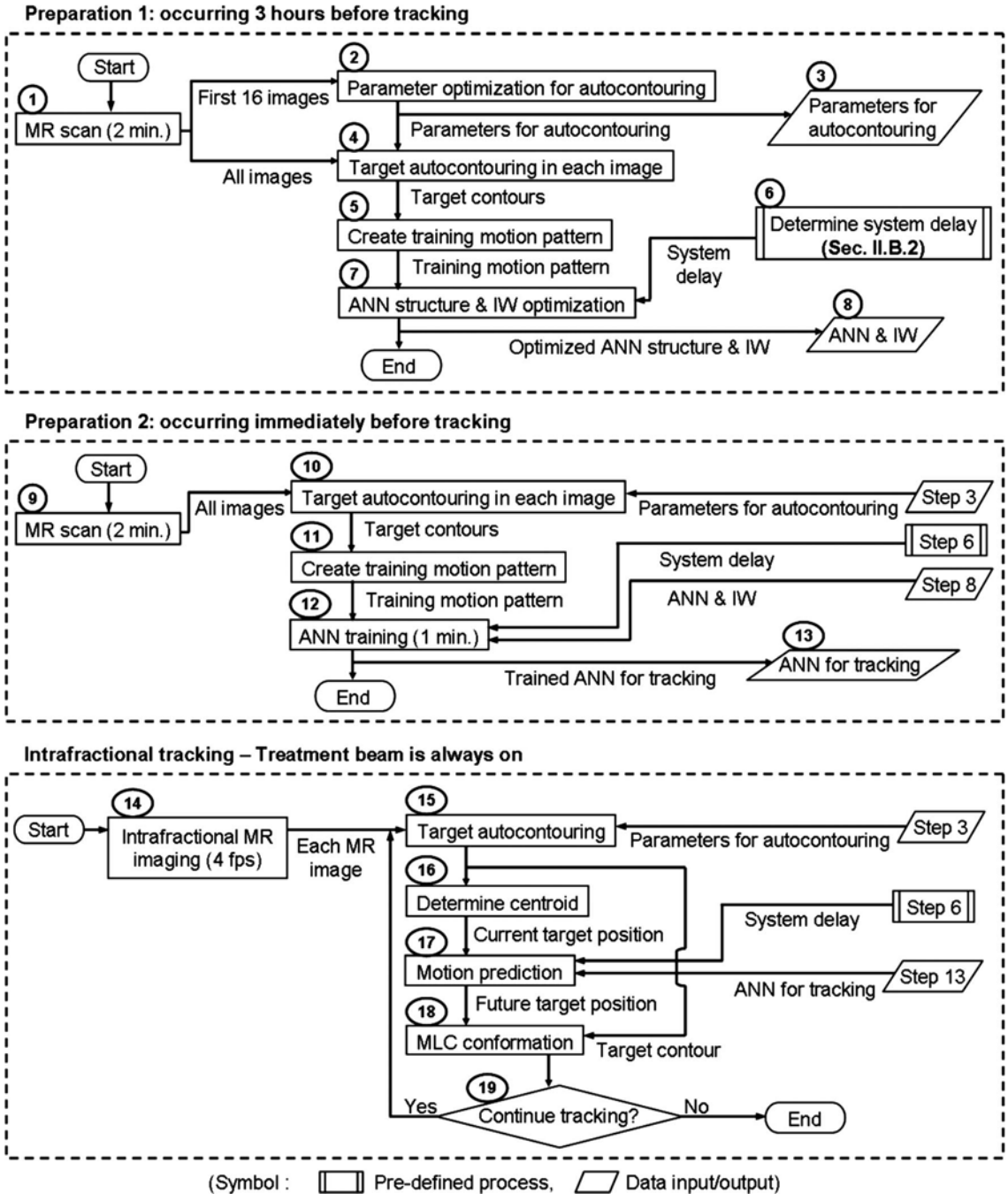

FIG. 4. Overview of intrafractional tumor tracking.

We developed motion prediction software to compensate for the tumor motion during system delay. Artificial neural networks (ANN) were used in this software to predict future tumor positions based on the previous ones. The performance of ANN is known to be strongly dependent on its structure and initial weights (IW).[33,34] That is, prediction accuracy of our software for a given patient's motion pattern might be very sensitive to the ANN. In our previous study using the recorded data of 29 lung cancer patients, the root mean squared error (RMSE) in motion prediction was reduced by 30%–60% when using patient specific ANN and IW compared to a single ANN and IW.[21] For this reason, ANN and IW are optimized and trained prior to motion prediction. More explanations on these processes follow in Secs. II.C.1 and II.C.2. As a result, we were able to use ANN for motion prediction, which was specifically optimized for a given motion pattern. Detailed software design and optimization process are presented in Yun *et al.*[21] Also, it is important to clarify that the prediction performance of our software does not depend on any relationship between the phase of motion and the timing of imaging event. There was no synchronization of the imaging clock and motion control in our experiments.

II.C. Methodology for intrafractional tracking

Figure 4 describes our tracking process, which was developed in accordance with the following scenario:

(1) Two sessions of pretracking MR scans are performed using the linac-MR as indicated in Steps 1 and 9 in Fig. 4. Both of these sessions proceed with the same MR sequence, phantom setup, and the motion pattern that would be used in the actual intrafractional tracking experiments.
(2) During tracking, the linac-MR provides 2D intrafractional, dynamic MR imaging of a target (Step 14). An MR imaging slice, perpendicular to the beam direction, with 30 mm thickness is selected to visualize the target as shown in Fig. 3(c). No synchronization is necessary between the phase of phantom motion and imaging sequences (i.e., intrafractional MR imaging may begin at a randomly chosen time point).

All of our software was coded in LabVIEW 2011 and executed on 32 bit computer system (Windows7, Intel i7-2600k, 4 GB RAM).

II.C.1. Preparation 1

In Preparation 1 (Steps 1–8 in Fig. 4), we optimize (1) parameters for the autocontouring software, and (2) the ANN structure and IW for motion prediction software. This occurs 3 h before tracking, which is the time requirement to execute Steps 1–8 in our computer system.

In Step 1, a pretracking MR scan is performed for 2 min at a 4 fps imaging rate, acquiring 480 images. In Step 2, the parameters required for the autocontouring software are optimized using the images from Step 1. We chose to use the first 16 images (4 s length) in Step 2, because 4 s is sufficient to cover the peak-to-peak movement of the phantom following the motion patterns used in this study. The target shown in each of these 16 images is manually contoured, and our software searches for the parameters that can produce an autocontoured target shape that is the most similar to the manual one in each image. Due to this algorithm, the accuracy of manual contouring is an important factor determining autocontouring performance. The manual contouring should be done by an expert user (e.g., radiation oncologists) if autocontouring were to be applied to *in vivo* images. In this study, however, accurate manual contouring was relatively easy due to the high contrast between the target and the background region. It is important to clarify that tumor contouring during the actual tracking session is fully automatic. Our software only uses the manual contours to arrive at the best parameters that will be used for autocontouring. The optimized parameters are stored in Step 3.

In Step 4, all images from Step 1 are autocontoured using the parameters from Step 2 in conjuction with the autocontouring software. In Step 5, our software (1) calculates the centroid position of the target from the autocontoured target shape in each image, and (2) records the centroid position in each image as a function of time. This record is referred as a training motion pattern as used in the motion prediction software. The training pattern, and the amount of system delay determined in Step 6 serve as input to Step 7 for the ANN structure and IW optimizations. Step 6 is explained earlier in Sec. II.B.2. In Step 8, an optimized ANN structure and IW are stored.

TABLE I. Summary of time requirements to perform Steps 1–13.

Process		Time
Preparation 1	First MR scan (Step 1)	2 min
	ANN optimization (Step 7)	~ 3 h
Preparation 2	Second MR scan (Step 9)	2 min
	ANN training (Step 12)	1 min
Total time requirement		~ 3 h

II.C.2. Preparation 2

In Preparation 2 (Steps 9–13 in Fig. 4), we further train the optimized ANN using the most recent tumor motion data. Preparation 2 occurs immediately prior to actual tumor tracking and takes approximately 3 min to complete.

In Step 9, a pretracking MR scan is performed for 2 min. In Steps 10 and 11, all images from Step 9 are autocontoured, and a training pattern is created. In Step 12, we train the ANN obtained from Step 8 for 1 min using the training pattern and system delay from Steps 11 and 6, respectively. The ANN is trained for approximately 10 000 epochs during 1 min, where one epoch refers to a single passing of a training pattern (prediction followed by weight corrections) through the ANN during iterative trainings. ANN training uses the training pattern solely derived from the image data and does not use the phantom motion encoder values. A detailed training process is presented in our previous publication.[21] The trained ANN is stored in Step 13. Table I provides the summary of time requirements to perform Steps 1–13.

II.C.3. Intrafractional tracking

The treatment beam is continuously on while Steps 14–19 in Fig. 4 are executed during intrafractional tracking. In Step 14, tracking begins with intrafractional MR imaging at 4 fps while the phantom is undergoing one of the two motion patterns simulating the tumor motion. Each MR image is autocontoured immediately after the acquisition in Step 15, using the parameters from Step 3.

In Step 16, our software determines the centroid position of the target contour, i.e., a current target position. This is input to Step 17 in order to predict a future target position. The prediction occurs using the ANN and system delay from Steps 13 and 6, respectively. For example, if the system delay is 500 ms, Step 17 will output a target position at 500 ms in the future.

In Step 18, the MLC conforms to the target contour at its predicted future position using the results from Steps 15 and 17. Here, the MLC leaf positions are determined as the

following: (1) the leaf positions are calculated to conform the MLC beam shape to the autocontoured target shape from Step 15, and (2) these leaf positions are shifted to translate the MLC shape to a future target position (i.e., centroid) obtained from Step 17. Depending on the result from Step 19, Steps 15–18 are iterated on each intrafractional MR image, or tracking is terminated.

It is important to note that Step 17, predicting the future tumor position, occurs at the same rate as the imaging frequency during tracking. This is because approximately the same amount of time (a few ms difference) is required to execute Steps 14–16 for each image. This result can be generalized to other imaging frequencies. Since each image was acquired at 4 fps (i.e., every 250 ms) in this study, the prediction occurred at the same rate, every 250 ms. If we use a different MR imaging rate for tracking; for example, 5 fps (i.e., every 200 ms), then the prediction will occur every 200 ms.

II.D. Demonstration of intrafractional tracking

We demonstrated intrafractional MR tumor tracking according to the four different scenarios shown in Table II. Each scenario was tested using two motion patterns as mentioned in Sec. II.A.4 with 2 min beam on time (100 MU/min).

Scenario 0 (S0) generates a "gold-standard" result, because radiation delivery to a static or moving target will be identical if we track the target perfectly. S0 was performed prior to each scenario, and the film exposed in other scenarios was registered and compared to the film from S0.

S1 simulates the situation of applying the maximum margin around the target covering the full extent of target motion. Thus, the wider, fixed beam will irradiate the moving target and the target is expected to remain inside the beam portal at all times. To demonstrate S1, we would ideally fix the Gafchromic film to measure the beam port with maximum margin and image the moving target in real-time using MRI. This requires physical separation of the film from the moving phantom, and the registration of film image with MR images to show that the target is always inside the beam. However, due to our phantom design where the film must travel with the phantom, we fixed the phantom at its equilibrium position and delivered radiation with the maximum beam margin to determine the beam width required to cover the moving target without tracking.

Scenarios S2–S4 are performed with the moving phantom. In S2, the MLC is conformed to the equilibrium target contour and location with no beam margin during beam delivery, representing radiation delivery without accounting for tumor motion. In S3, MLC tracking is enabled without motion prediction, i.e., beam follows the phantom motion without motion prediction capability. In S4, the motion prediction feature is enabled in addition to MLC tracking. The last scenario represents the mode of operation envisaged for future clinical systems.

TABLE II. Tracking scenarios.

	Scenario 0 (S0)	S1	S2	S3	S4
Phantom motion	No	No	Yes	Yes	Yes
Beam margin	None	Maximum	None	None	None
MLC tracking	No	No	No	Yes	Yes
Motion prediction	No	No	No	No	Yes

II.E. Tracking accuracy evaluation

We evaluated the tracking accuracy of each scenario using the following methods:

(1) Observing encoder readings of phantom and MLC: During tracking experiments, we recorded encoder readings from phantom and MLC every 50 ms. As explained earlier, there was no synchronization of the imaging clock and the phase of phantom motion in our experiments. Using the encoder readings, we plotted the position changes of the phantom and MLC during tracking as a function of time, and observed the time difference between the two curves in each scenario. The time difference here should ideally be zero if the tracking is perfect.
(2) Film measurements: There was no difference in total time spent in generating the films for each of the scenarios. All films were digitized approximately 12 h after exposure, using a VIDAR VXR film digitizer (VIDAR Systems Corporation, Herndon, VA) at 0.36 $\times$ 0.36 mm^2 resolution. The digitized optical density was converted to dose (cGy) using our inhouse developed software.[35] We then compared (1) 80%–20% penumbra width (i.e., the distance between two points receiving 80% and 20% of the maximum dose), and (2) beam width at 50% of the maximum dose in each scenario. These were calculated from the profiles as indicated in Fig. 6.

III. RESULTS

III.A. Encoder readings of phantom and MLC

We monitored and recorded the positional changes of the phantom and each MLC leaf during tracking through encoder readings. This yielded 11 sets of motion data (1 from the phantom encoder, 10 from the MLC encoder). As explained earlier, all encoder readings were taken at the same instance every 50 ms and time-stamped. These motion data were normalized and plotted as a function of time. From these, we calculated the MLC encoder reading shown in Fig. 5, which is an average of five encoder readings from Encoder-R in Fig. 1(a). The averaging was performed due to the following reason. Although we tracked the rigid target undergoing translational motion, there exist slight motor-to-motor variations in encoder readings, because (1) each motor drives each MLC leaf conforming to the autocontoured target shape, and (2) the autocontoured target shape can slightly change, within 1 pixel on the edges, as the quality of intrafractional MR images are not identical during tracking experiments. This caused approximately 2% variation in target size among the

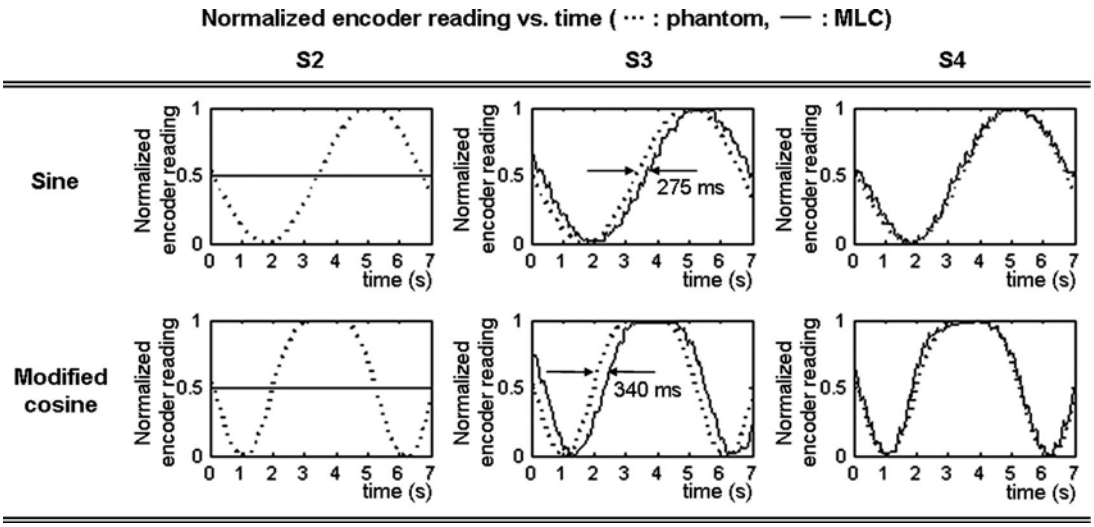

FIG. 5. Encoder reading comparisons from phantom and MLC (recorded every 50 ms during tracking). The readings correspond to scenarios S2–S4 and the two motion patterns are shown.

images. Nevertheless, because the variability of the five encoder readings was small (∼ 3%), we reported the average of five encoder readings to provide better representation of MLC motions as a whole in Fig. 5.

In S2 plots (sine and modified cosine) shown in Fig. 5, dotted lines indicate phantom motions following both motion patterns. There is no MLC motion in S2, therefore the encoder reading is represented as a straight line.

To find the amount of system delay, we performed tumor tracking without a motion prediction capability. S3 plots in Fig. 5 show the position changes of the phantom and MLC during this test in both motion patterns, and we calculated system delay from the time difference between the two curves. For example, in case of the sine pattern, the S3 plot shows constant lagging of MLC motion curve behind the phantom motion curve. The two motion curves were best matched when shifted by 275 ms, which is the amount of system delay. The same method was used to calculate 340 ms system delay in the modified cosine pattern. The difference in the amount of system delays is due to different target speeds (maximum speed of 1.8 and 3.1 cm/s in sine and modified cosine patterns, respectively); hence, different time requirements for MLC tracking in two motion patterns. Using these system delay values, our motion prediction software was optimized and trained for each motion pattern prior to tracking as explained in Sec. II.C.1.

S4 plots show no observable time difference between the two curves, indicating the phantom motion during system delay is more accurately tracked by the MLC due to the enabling of the motion prediction feature.

III.B. Film measurement

Figure 6 shows the films exposed in different tracking scenarios (S0–S4). S0 was performed prior to each scenario, and each film exposed in S1–S4 was registered to the film from S0 using surrogates markers as explained in Sec. II.A.2. All films were digitized, and their optical density values were converted to dose (cGy). Dose profiles were calculated along the white dashed line indicated in Fig. 6. The open beam dose profiles are not flat due to a slight misalignment of the beam and the flattening filter in the linac-MR. The dose rates are similar to those of clinical 600 C units (50, 100, 150, 200, 250 cGy/min at isocenter).

In S1, the target is fully irradiated, but much larger volume than the designed target in this experiment is irradiated. In S2, the amount of unnecessary dose is decreased. However, we cannot deliver sufficient dose to the target.

In S3, unnecessary dose to surrounding region is substantially decreased by enabling tracking feature. However, there still exist hot and cold spots, and general mismatch of penumbra, when comparing S0 and S3 dose profiles. This is due to target motions during system delay, which will be increased as the speed of target motion increases. Comparing S3 dose profiles from both motion patterns, the area of hot and cold spots and penumbra mismatch are larger when we use the modified cosine pattern which has a faster target speed.

In S4, we delivered highly conformal dose to the moving target by adding a motion prediction feature. Dose profiles between static and moving target cases show good agreement in both motion patterns. It should be noted that no margin for target motion is included in scenarios S2–S4.

From visual inspection, the shape of the high dose region covering the target in S4 films show the sharpest edges compared to the blurred ones shown in S2 and S3 films. In Table III, we compared (1) beam width at 50%, and (2) 80%–20% penumbra width from the dose profile in each tracking scenario. Here, S0 values are averaged from all S0 dose profiles shown in Fig. 6.

The measured value of 50% beam width stays within ±1 mm in all scenarios except S1 that represents the deliberately introduced geometric margin to account for the target motion. The measured value of 80%–20% penumbra width is increased up to 27 mm in S2 and 9 mm in S3 compared to

TABLE III. Beam and penumbra width in different scenarios.

Phantom motion	None		Sine			Modified cosine		
Tracking scenario	S0	S1	S2	S3	S4	S2	S3	S4
50% beam width (mm)	62.5	103.4	63.5	62.4	62.0	63.6	61.9	62.2
80%–20% penumbra width (mm)	6.9	7.0	33.0	11.5	7.3	34.1	15.8	8.6

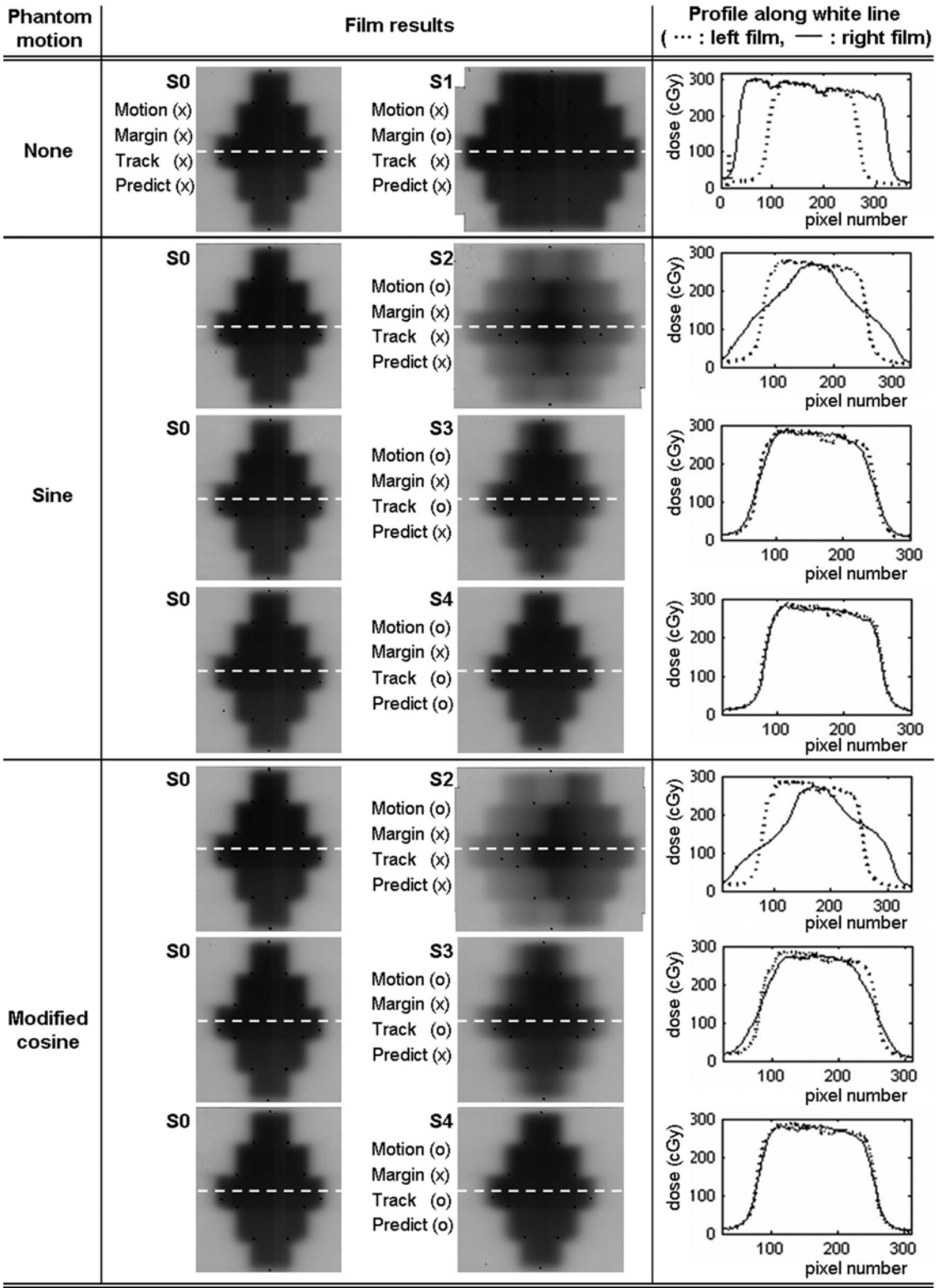

FIG. 6. Film measurement in different scenarios using the sine and modified cosine motion patterns.

S0. In S4, however, the increase in penumbra width is limited to 0.4 and 1.7 mm in the sine and modified cosine patterns, respectively.

IV. DISCUSSION

This study presents the first demonstration of intrafractional tumor tracking using 2D MR images. Using a prototype linac-MR, our tracking system automatically tracks the motion and delivers radiation onto the moving target. The MRI-guided tumor tracking study by Crijns *et al.*[36] does not perform intrafractional 2D imaging of the tumor and does not address the system delay, discussed in Sec II.B.2, introduced mainly by the MLC motion.

The dosimetric advantage of intrafractional tracking in treating mobile tumors is clearly shown in Fig. 6. Using our tracking method, we delivered highly conformal dose to a moving target simulating 1D lung-tumor motions in SI direction. Compared to static target irradiation, 50% beam width remained within 0.5 mm, and the 80%–20% penumbra width increased by 0.4 and 1.7 mm in moving target irradiations using the sine and modified cosine motion patterns, respectively. The difference in penumbra width in these two motion patterns arises due to the maximum target speed, 1.8 and 3.1 cm/s at maximum, respectively. These results are applicable to the current phantom and experimental situation. Further investigations are required to demonstrate the proper operation of our tracking system with the patient or patient like situations. Also, for the same reason, it is difficult to discuss the impact of our results on an intensity-modulated radiation therapy (IMRT) delivery at current stage, even though several studies have discussed applying IMRT combined with real-time tracking capability.[37–40]

Various prediction algorithms including using ANN have been proposed to compensate for tumor motion during system delay.[41–44] Although it would be interesting to incorporate these previously developed algorithms in our tracking system and compare the results, the following main problem exists in reality: all previously developed algorithms assumed the tumor position detection at 30 Hz by monitoring the position of tumor surrogates using optical tracking devices, or a stereoscopic x-ray fluoroscopy system. However, current MR imaging can typically achieve image acquisition rates of 3–4 fps. Due to this significant difference in detection rates, we had to develop a new algorithm designed specifically for MR-based tumor tracking. This report presents the tumor tracking performance achieved by using our prediction algorithm. If a new algorithm for MR-based tracking is developed in future, then a comparison study can be performed.

Our motion prediction algorithm functioned well in our tracking system, where a large amount of system delay is inevitable due to MR image acquisition and image processing time. We expect that our algorithm will also function for other non-MRI based modern tracking systems, which should have much shorter system delay time without having to perform MR imaging. The system delay in a real clinical system can be determined by either of the following two methods: (1) a pretreatment MR scan will provide tumor motions in several breathing cycles. The phantom can then be programmed to undergo this motion pattern and the system delay can be determined using the same method as described in Sec. II.B.2; (2) the system delay mainly depends on tumor speed. Thus, a lookup table of system delay can be created as a function of tumor speed. The patient specific system delay can then be looked up from this table based on the patient's tumor speed obtained from the pretreatment MR scan.

We used the motion patterns that are stable and perfectly periodic in this study. However, it is unreasonable to expect such high reproducibility in patient breathing motions. This inevitable challenge will mainly affect the motion prediction performance of the tracking system. To minimize the errors in motion prediction due to inter- or intrafractional instability of motion patterns, the following two features are implemented in our motion prediction software: (1) to deal with interfractional motion changes, the software was designed to reoptimize its ANN for each fraction of the treatment. In this process, the tumor motion data recorded from a previous fraction are used as a training motion pattern, presuming that tumor motions in two consecutive fractions are the most similar; (2) to deal with intrafractional motion changes, adaptive learning is incorporated in the software by continuously updating the weights and learning rate (η) of a given ANN during motion prediction in real-time. The weights and η represent the knowledge and convergence rate of ANN, respectively. More explanations can be found in Haykin.[45] In this way, the ANN's learning process is not limited to the training session alone but continues during the actual tracking session, and our predictor can adapt to the intrafractional changes in motion pattern to a certain degree.

Because accurate motion prediction is essential for successful intrafractional tracking, we evaluated the prediction performance of our software using realistic lung-tumor motions in our previous study.[21] Here, the 1D superior-inferior lung-tumor motions of 29 lung cancer patients were used to test our software for various system delays of 120–520 ms, in increments of 80 ms. For 280 and 360 ms system delays that are more relevant to this study, mean RMSE values of 0.7 and 0.8 mm (ranges 0.1–2.5 mm) were observed, respectively. Proving these results through actual tracking experiments using realistic lung-tumor motions will be a subject of future study.

We focused on tracking 1D translational motions of a rigid target in this study. Real tumor motion, however, includes translation, rotation, as well as volume changes. For example, lung-tumor shows 3D displacement with volume changes and rotational motions during normal breathing. Hence, the next step will be demonstrating more realistic tumor tracking in 3D space. Currently, we can accomplish 2D MR imaging with 4 fps imaging rate to track lung-tumor motions. However, a potential problem that can arise is through plane tumor motion (motion orthogonal to the imaging plane), even though numerous studies have demonstrated that the largest lung-tumor motions occur in SI directions. Potential solutions to this problem could be adjusting the orientation and slice thickness of the imaging plane to capture the SI directional

tumor motion and ensure the tumor remains in the imaging plane.

Tumor shape deformation during beam delivery due to rotation, volume changes, and other reasons is another challenge. To evaluate tracking performance in these situations, we must develop an MRI compatible, deformable motion phantom that has accurate deformation reproducibility. This requires simultaneous implementation of known patterns of motion and deformation. The phantom used in this study contains a simulated target of rigid shape in order to show practicality of tracking. Nevertheless, our tracking system is not limited to rigid body tracking. Our tracking method is based on (1) determining both the shape and location of the target from each MR image, and (2) reshaping and moving the MLC accordingly in real-time. To achieve this, our autocontouring software was designed to deal with possible deformations of the tumor shape, and it contours each image individually without the need of *a priori* assumptions regarding tumor shape or contrast. The autocontouring performance of the software used in this study was previously evaluated through a phantom study (circular and noncircular tumor shapes),[20] as well as an *in vivo* study.[46] In both studies, autocontoured targets/tumors were compared to standard, manual contours. Here, it was shown that the autocontouring accuracy decreases with lower contrast-to-noise ratio (CNR) of the target/tumor in MR images. Nevertheless, if CNR >5, autocontours have an average centroid displacement <1 and <2 mm, as well as Dice's coefficient $>93\%$ and $>83\%$ compared to the standard contours in the phantom and *in vivo* study, respectively. This might be an indication of the CNR level required for successful autocontouring; however, more investigation is needed to evaluate the software performance with deformable target shapes. This future study will include developing a deformable phantom.

This study was carried out to demonstrate the technical aspect of MRI based tracking using a phantom. Current phantom design and target shape were decided considering several factors including MLC leaf width, prototype linac-MR geometry, and RF coil size. The phantom may represent a more suitable condition for contrast in the images as it does not include the susceptibility issues occurring at the air-tissue interface of human lung. Further studies using realistic phantoms, human volunteers, and/or patients are required.

V. CONCLUSION

We have demonstrated intrafractional MR tumor tracking using a prototype linac-MR. An MR compatible motion phantom was used to simulate tumor motions during 2 min of irradiation. Different tumor tracking scenarios were tested with two different phantom motion patterns.

We delivered highly conformal dose to a moving target using predictive tumor tracking. Compared to static target irradiation, 50% beam width remains virtually unchanged, <0.5 mm, and the increase in 80%–20% penumbra width is less than 1.7 mm in moving target irradiation. These results illustrate potential dosimetric advantages of intrafractional MR tumor tracking in treating mobile tumors as shown for the phantom case.

[a]Electronic mail: Gino.Fallone@albertahealthservices.ca

[1]M. B. Tacke, S. Nill, A. Krauss, and U. Oelfke, "Real-time tumor tracking: Automatic compensation of target motion using the Siemens 160 MLC," Med. Phys. **37**(2), 753–761 (2010).
[2]A. Sawant, R. L. Smith, R. B. Venkat, L. Santanam, B. C. Cho, P. Poulsen, H. Cattell, L. J. Newell, P. Parikh, and P. J. Keall, "Toward submillimeter accuracy in the management of intrafraction motion: The integration of real-time internal position monitoring and multileaf collimator target tracking," Int. J. Radiat. Oncol., Biol., Phys. **74**(2), 575–582 (2009).
[3]B. Cho, P. R. Poulsen, A. Sloutsky, A. Sawant, and P. J. Keall, "First demonstration of combined kV/MV image-guided real-time dynamic multileaf-collimator target tracking," Int. J. Radiat. Oncol., Biol., Phys. **74**(3), 859–867 (2009).
[4]A. Krauss, S. Nill, M. Tacke, and U. Oelfke, "Electromagnetic real-time tumor position monitoring and dynamic multileaf collimator tracking using a Siemens 160 MLC: Geometric and dosimetric accuracy of an integrated system," Int. J. Radiat. Oncol., Biol., Phys. **79**(2), 579–587 (2011).
[5]S. S. Vedam, V. R. Kini, P. J. Keall, V. Ramakrishnan, H. Mostafavi, and R. Mohan, "Quantifying the predictability of diaphragm motion during respiration with a noninvasive external marker," Med. Phys. **30**(4), 505–513 (2003).
[6]E. Nioutsikou, Y. Seppenwoolde, J. R. N. Symonds-Tayler, B. Heijmen, P. Evans, and S. Webb, "Dosimetric investigation of lung tumor motion compensation with a robotic respiratory tracking system: An experimental study," Med. Phys. **35**(4), 1232–1240 (2008).
[7]T. Harada, H. Shirato, S. Ogura, S. Oizumi, K. Yamazaki, S. Shimizu, R. Onimaru, K. Miyasaka, M. Nishimura, and H. Dosaka-Akita, "Real-time tumor-tracking radiation therapy for lung carcinoma by the aid of insertion of a gold marker using bronchofiberscopy," Cancer **95**(8), 1720–1727 (2002).
[8]K. Kitamura, H. Shirato, S. Shimizu, N. Shinohara, T. Harabayashi, T. Shimizu, Y. Kodama, H. Endo, R. Onimaru, S. Nishioka, H. Aoyama, K. Tsuchiya, and K. Miyasaka, "Registration accuracy and possible migration of internal fiducial gold marker implanted in prostate and liver treated with real-time tumor-tracking radiation therapy (RTRT)," Radiother. Oncol. **62**(3), 275–281 (2002).
[9]M. Imura, K. Yamazaki, H. Shirato, R. Onimaru, M. Fujino, S. Shimizu, T. Harada, S. Ogura, H. Dosaka-Akita, K. Miyasaka, and M. Nishimura, "Insertion and fixation of fiducial markers for setup and tracking of lung tumors in radiotherapy," Int. J. Radiat. Oncol., Biol., Phys. **63**(5), 1442–1447 (2005).
[10]D. Ionascu, S. B. Jiang, S. Nishioka, H. Shirato, and R. I. Berbeco, "Internal-external correlation investigations of respiratory induced motion of lung tumors," Med. Phys. **34**(10), 3893–3903 (2007).
[11]D. P. Gierga, J. Brewer, G. C. Sharp, M. Betke, C. G. Willett, and G. T. Y. Chen, "The correlation between internal and external markers for abdominal tumors: Implications for respiratory gating," Int. J. Radiat. Oncol., Biol., Phys. **61**(5), 1551–1558 (2005).
[12]L. Ekberg, O. Holmberg, L. Wittgren, G. Bjelkengren, and T. Landberg, "What margins should be added to the clinical target volume in radiotherapy treatment planning for lung cancer?," Radiother. Oncol. **48**(1), 71–77 (1998).
[13]J. V. Frangioni, "New technologies for human cancer imaging," J. Clin. Oncol. **26**(24), 4012–4021 (2008).
[14]V. S. Khoo and D. L. Joon, "New developments in MRI for target volume delineation in radiotherapy," Br. J. Radiol. **79**(Special Issue 1), S2–S15 (2006).
[15]L. A. Dawson and C. Menard, "Imaging in radiation oncology: A perspective," Oncologist **15**(4), 338–349 (2010).
[16]J. H. Jonsson, M. G. Karlsson, M. Karlsson, and T. Nyholm, "Treatment planning using MRI data: An analysis of the dose calculation accuracy for different treatment regions," Radiat. Oncol. **5**, 62–69 (2010).
[17]B. G. Fallone, B. Murray, S. Rathee, T. Stanescu, S. Steciw, S. Vidakovic, E. Blosser, and D. Tymofichuk, "First MR images obtained during megavoltage photon irradiation from a prototype integrated linac-MR system," Med. Phys. **36**(6), 2084–2088 (2009).
[18]J. Yun, J. St. Aubin, S. Rathee, and B. G. Fallone, "Brushed permanent magnet DC MLC motor operation in an external magnetic field," Med. Phys. **37**(5), 2131–2134 (2010).

[19]M. Lamey, J. Yun, S. Rathee, and B. G. Fallone, "Radio frequency noise from an MLC: A feasibility study of the use of an MLC for linac-MR systems," Phys. Med. Biol. **55**(4), 981–994 (2010).
[20]J. Yun, E. Yip, K. Wachowicz, S. Rathee, M. Mackenzie, D. Robinson, and B. G. Fallone, "Evaluation of a lung tumor autocontouring algorithm for intrafractional tumor tracking using low-field MRI: A phantom study," Med. Phys. **39**(3), 1481–1494 (2012).
[21]J. Yun, M. Mackenzie, S. Rathee, D. Robinson, and B. G. Fallone, "An artificial neural network (ANN)-based lung-tumor motion predictor for intrafractional MR tumor tracking," Med. Phys. **39**(7), 4423–4433 (2012).
[22]C. Plathow, C. Fink, S. Ley, M. Puderbach, M. Eichinger, I. Zuna, A. Schmahl, and H. U. Kauczor, "Measurement of tumor diameter-dependent mobility of lung tumors by dynamic MRI," Radiother. Oncol. **73**(3), 349–354 (2004).
[23]H. Shirato, K. Suzuki, G. C. Sharp, K. Fujita, R. Onimaru, M. Fujino, N. Kato, Y. Osaka, R. Kinoshita, H. Taguchi, S. Onodera, and K. Miyasaka, "Speed and amplitude of lung tumor motion precisely detected in four-dimensional setup and in real-time tumor-tracking radiotherapy," Int. J. Radiat. Oncol., Biol., Phys. **64**(4), 1229–1236 (2006).
[24]H. Shirato, Y. Seppenwoolde, K. Kitamura, R. Onimura, and S. Shimizu, "Intrafractional tumor motion: Lung and liver," Semin. Radiat. Oncol. **14**(1), 10–18 (2004).
[25]C. Plathow, M. Schoebinger, C. Fink, H. Hof, J. Debus, H. P. Meinzer, and H. U. Kauczor, "Quantification of lung tumor volume and rotation at 3D dynamic parallel MR imaging with view sharing: Preliminary results," Radiology **240**(2), 537–545 (2006).
[26]P. J. Keall, G. S. Mageras, J. M. Balter, R. S. Emery, K. M. Forster, S. B. Jiang, J. M. Kapatoes, D. A. Low, M. J. Murphy, B. R. Murray, C. R. Ramsey, M. B. Van Herk, S. S. Vedam, J. W. Wong, and E. Yorke, "The management of respiratory motion in radiation oncology report of AAPM Task Group 76," Med. Phys. **33**(10), 3874–3900 (2006).
[27]S. S. Lo, B. S. Teh, J. J. Lu, and T. E. Schefter, *Stereotactic Body Radiation Therapy* (Springer-Verlag, Berlin, 2012).
[28]M. A. Bernstein, K. F. King, and X. J. Zhou, *Handbook of MRI Pulse Sequences* (Academic, Burlington, MA, 2004).
[29]M. L. Taylor, R. L. Smith, F. Dossing, and R. D. Franich, "Robust calculation of effective atomic numbers: The Auto-Zeff software," Med. Phys. **39**(4), 1769–1778 (2012).
[30]S. Rajaram, A. J. Swift, D. Capener, A. Telfer, C. Davies, C. Hill, R. Condliffe, C. Elliot, J. Hurdman, D. G. Kiely, and J. M. Wild, "Lung morphology assessment with balanced steady-state free precession MR imaging compared with CT," Radiology **263**(2), 569–577 (2012).
[31]A. E. Lujan, E. W. Larsen, J. M. Balter, and R. K. Ten Haken, "A method for incorporating organ motion due to breathing into 3D dose calculations," Med. Phys. **26**(5), 715–720 (1999).
[32]Y. Tsunashima, T. Sakae, Y. Shioyama, K. Kagei, T. Terunuma, A. Nohtomi, and Y. Akine, "Correlation between the respiratory waveform measured using a respiratory sensor and 3D tumor motion in gated radiotherapy," Int. J. Radiat. Oncol., Biol., Phys. **60**(3), 951–958 (2004).
[33]H. R. Maier and G. C. Dandy, "The effect of internal parameters and geometry on the performance of back-propagation neural networks: an empirical study," Environ. Modell. Softw. **13**(2), 193–209 (1998).
[34]L. F. A. Wessels and E. Barnard, "Avoiding false local minima by proper initialization of connections," IEEE Trans. Neural Networks **3**(6), 899–905 (1992).
[35]S. D. Thomas, M. Mackenzie, G. C. Field, A. M. Syme, and B. G. Fallone, "Patient specific treatment verifications for helical tomotherapy treatment plans," Med. Phys. **32**(12), 3793–3800 (2005).
[36]S. P. M. Crijns, B. W. Raaymakers, and J. J. W. Lagendijk, "Proof of concept of MRI-guided tracked radiation delivery: Tracking one-dimensional motion," Phys. Med. Biol. **57**(23), 7863–7872 (2012).
[37]L. Papiez, D. Rangaraj, and P. Keall, "Real-time DMLC IMRT delivery for mobile and deforming targets," Med. Phys. **32**(9), 3037–3048 (2005).
[38]Y. L. Suh, A. Sawant, R. Venkat, and P. J. Keall, "Four-dimensional IMRT treatment planning using a DMLC motion-tracking algorithm," Phys. Med. Biol. **54**(12), 3821–3835 (2009).
[39]R. L. Smith, A. Sawant, L. Santanam, R. B. Venkat, L. J. Newell, B. C. Cho, P. Poulsen, H. Catell, P. J. Keall, and P. J. Parikh, "Integration of real-time internal electromagnetic position monitoring coupled with dynamic multileaf collimator tracking: An intensity-modulated radiation therapy feasibility study," Int. J. Radiat. Oncol., Biol., Phys. **74**(3), 868–875 (2009).
[40]D. McQuaid, M. Partridge, J. R. N. Symonds-Tayler, P. M. Evans, and S. Webb, "Experimental validation of a target tracking IMRT delivery with conventional MLCs," Clin. Oncol. **21**(3), 243–244 (2009).
[41]G. C. Sharp, S. B. Jiang, S. Shimizu, and H. Shirato, "Prediction of respiratory tumour motion for real-time image-guided radiotherapy," Phys. Med. Biol. **49**(3), 425–440 (2004).
[42]A. Krauss, S. Nill, and U. Oelfke, "The comparative performance of four respiratory motion predictors for real-time tumour tracking," Phys. Med. Biol. **56**(16), 5303–5317 (2011).
[43]J. H. Goodband, O. C. L. Haas, and J. A. Mills, "A comparison of neural network approaches for on-line prediction in IGRT," Med. Phys. **35**(3), 1113–1122 (2008).
[44]M. J. Murphy and D. Pokhrel, "Optimization of an adaptive neural network to predict breathing," Med. Phys. **36**(1), 40–47 (2009).
[45]S. S. Haykin, *Neural Networks: A Comprehensive Foundation* (Prentice-Hall, Upper Saddle River, NJ, 1999).
[46]E. Yip, J. Yun, Z. Gabos, K. Wachowicz, S. Rathee, and B. G. Fallone, "Evaluation of a real time tumour autocontouring algorithm using *in-vivo* lung MR images with various contrast to noise ratios," presented at the *54th Annual Meeting of the AAPM, Charlotte, NC*, 29 July–2 August, 2012.